

CHANDRA OBSERVATION OF THE CENTRAL REGION OF THE COOLING FLOW CLUSTER
ABELL 262: A RADIO SOURCE THAT IS A SHADOW OF ITS FORMER SELF?

ELIZABETH L. BLANTON^{1,2}, CRAIG L. SARAZIN¹, BRIAN R. MCNAMARA³ AND T. E. CLARKE¹
Astrophysical Journal, in press

ABSTRACT

We present a *Chandra* observation of the cooling flow cluster Abell 262. Spectral fits show that the intracluster medium (ICM) in A262 cools by a factor of three from 2.7 keV to 0.9 keV at the cluster center. A mass deposition rate of $\dot{M} = 19_{-5}^{+6} M_{\odot} \text{ yr}^{-1}$ is measured. Complex structure is found in the very inner regions of the cluster, including knots of emission and a clear deficit of emission to the east of the cluster center. The bright X-ray structures are located in the same regions as optical line emission, indicating that cooling to low temperatures has occurred in these regions. The X-ray deficit is spatially coincident with the eastern radio lobe associated with the active galactic nucleus hosted by the central cD galaxy. The region surrounding the X-ray hole is cool, and shows no evidence that it has been strongly shocked. This joins the ranks of other cooling flow clusters with *Chandra*-detected bubbles blown by central radio sources. This source is different than the other well-known cases, in that the radio source is orders of magnitude less luminous and has produced a much smaller bubble. Comparing the energy output of the radio source with the luminosity of the cooling gas shows that energy transferred to the ICM from the radio source is insufficient to offset the cooling flow unless the radio source is currently experiencing a less powerful than average outburst, and was more powerful in the past.

Subject headings: cooling flows — galaxies: clusters: general — galaxies: clusters: individual (Abell 262) — intergalactic medium — radio continuum: galaxies — X-rays: galaxies: clusters

1. INTRODUCTION

Recent X-ray observations from the *Chandra* and *XMM-Newton* Observatories have shed much light on the physical state of the intracluster medium (ICM) in clusters of galaxies. Gas is predicted to cool first in the dense centers of clusters of galaxies since the cooling time varies as $t_{\text{cool}} \propto T^{1/2}/n_e$, where T is the gas temperature and n_e is the electron number density. In order to maintain hydrostatic equilibrium, gas then flows into the cluster center to make up for the pressure lost from the cooling gas. Evidence for these “cooling flows” (see Fabian et al. 1994 for a review) was seen with observations with the *Einstein* (White 1992), *ROSAT* (Peres et al. 1998), and *ASCA* (White 2000) observatories. These observations predicted hundreds of solar masses of gas per year would flow into the centers of clusters and cool. The main problem with this picture was that sufficiently large quantities of cool gas were not inferred from observations taken at other wavelengths. While increased star formation was observed in the centers of cD galaxies in the centers of cooling flow clusters, as compared with non-cooling flows, the rates measured did not match the cooling rates derived from the X-ray observations (McNamara 1997).

Analysis of high-resolution spectroscopic data from *XMM-Newton* has revealed that the majority of the cooling X-ray-emitting ICM in the centers of cooling flows is cooling only over a limited temperature range, down to approximately one-half or one-third of the temperature in the outer regions of the cluster (Peterson et al. 2003). Temperature profiles measured with *Chandra* data have shown

a similar phenomenon (McNamara et al. 2000; Johnstone et al. 2002; Blanton et al. 2001, 2003). In addition, the mass-deposition rates measured with both *XMM-Newton* and *Chandra* are lower than the rates found with the earlier observatories. Various scenarios have been proposed to explain the new results including thermal conduction, inhomogeneous abundances, mixing, and heating of the cooling ICM by a central radio source (see Fabian et al. 2001; Peterson et al. 2001).

Remarkable high-resolution images from the *Chandra* X-ray Observatory have revealed in great detail the profound effect that radio sources associated with the central bright elliptical galaxies have on the X-ray-emitting ICM. The radio sources evacuate cavities (or “blow bubbles”) in the ICM, creating holes in the X-ray emission (e.g. Hydra A, McNamara et al. 2000; Perseus, Fabian et al. 2000; A2052, Blanton et al. 2001). These bubbles rise buoyantly, transporting energy and magnetic fields into the ICM (as in Perseus, Fabian et al. 2000; A2597, McNamara et al. 2001). Theoretical models had predicted that the radio sources would directly heat the ICM through strong shocks (Heinz, Reynolds, & Begelman 1998). However, in all observations of cooling flow clusters with central radio sources to date, no evidence of strong-shock heating has been found. In fact, the dense rims around the bubbles have been found to be cool, not hot, as would be predicted from a strong shock (Schmidt et al. 2002; Nulsen et al. 2002; Blanton et al. 2003). More recent models (Reynolds, Heinz, & Begelman 2002) have found that weak shocks occurring some time in the past are consistent with the ob-

¹ Department of Astronomy, University of Virginia, P. O. Box 3818, Charlottesville, VA 22903-0818; eblanton@virginia.edu, sarazin@virginia.edu, tclarke@virginia.edu

² *Chandra* Fellow

³ Department of Physics & Astronomy, Ohio University, Clipping Labs, Athens, OH 45701; mcnamara@helios.phy.ohiou.edu

servations (see also Soker, Blanton, & Sarazin 2002). For example, recent observational evidence of weak shock features have been found in Perseus (Fabian et al. 2003) and M87/Virgo (Forman et al. 2004). Comparisons of the total power emitted from the central radio source with the luminosity of cooling gas have shown that the energy emitted from a central radio source is sufficient to offset the cooling of the ICM in the centers of clusters, at least in some cases (e.g. Hydra A, David et al. 2001; A2052, Blanton et al. 2003). The details of the transportation of the radio source energy to the ICM are somewhat unclear thus far; however, the scenario of radio source heating remains a promising solution for the problem of the missing cool gas in the cooling flow model.

In this paper, we present *Chandra* data of the cooling flow cluster Abell 262. We focus on the central region of the cluster and the interaction between the radio source and the X-ray-emitting intracluster medium. Larger-scale properties of the cluster will be presented in a future paper (Blanton et al., in preparation). Abell 262 is a member of the Perseus supercluster, along with the Perseus cluster (Abell 426) and Abell 347. It is at a redshift of 0.0163 and is a richness class 0 cluster. The central cD galaxy, NGC 708, is host to a double-lobed radio source, B2 0149+35 (Parma et al. 1986; Fanti et al. 1987). A262 was previously observed in the X-ray with *Einstein* (David et al. 1993), *ROSAT* (David, Jones, & Forman 1996; Peres et al. 1998; Neill et al. 2001), *ASCA* (White 2000), and *XMM-Newton* (Peterson et al. 2003). The *ASCA* data gave an average temperature of $kT = 2.3$ keV and an average chemical abundance of 0.3 times the solar value. The *Einstein* data gave a bolometric luminosity of $L_{X,\text{bol}} = 4.4 \times 10^{43}$ erg s^{-1} , scaled to our cosmology (see below). Previous values of the mass deposition rate are $\dot{M} = 13^{+14}_{-13} M_{\odot}$ (spectral fit with *ASCA*; White 2000) and $\dot{M} = 14^{+2}_{-2} M_{\odot}$ (morphological determination from *ROSAT*, Peres 1998), scaled to our cosmology. Using *XMM-Newton* data, Peterson et al. (2003) found $\dot{M} = 10 \pm 1 M_{\odot}$ in the range kT to $kT/2$ where $kT = 2.1 \pm 0.2$ is the temperature of the ICM outside of the cooling region. We assume $H_0 = 70$ km s^{-1} Mpc $^{-1}$, $\Omega_M = 0.3$, and $\Omega_{\Lambda} = 0.7$ throughout. At $z = 0.0163$, $D_L = 70.7$ Mpc and $1'' = 0.3318$ kpc. Unless otherwise noted, all error bars are 90% confidence regions.

2. OBSERVATION AND DATA REDUCTION

Abell 262 was observed with the *Chandra* X-ray Observatory on 2001 August 3 for a total of 28,743 seconds. The cluster center was positioned one arcmin away from the nominal pointing of the ACIS-S3 detector to avoid a node boundary on the chip. The events were telemetered in very faint (VF) mode, with an energy filter of 0.1-13 keV to avoid saturation during telemetry. The data were collected with frame times of 3.2 seconds and the CCD temperature was -120 C. Only events with *ASCA* grades of 0, 2, 3, 4, and 6 were included. In addition to the S3, we received data from the S1, S2, S4, and I3 CCDs. We include data from the S3 only in our analysis. Data from the S1 are used to check for background flares.

We used the data analysis package CIAO v2.2 for the data reductions. Background files were taken from the blank sky observations of M. Markevitch⁴ included in

the CIAO calibration database (CALDB). Since VF-mode blank-sky observations with the ACIS-S3 were not available at the time of our analysis, we processed the data in Faint (F) mode, to be consistent with the background data. Bad pixels, bad columns, and columns next to bad columns and node boundaries were excluded. For the analysis, event PI values and photon energies were determined using the `acisD2000-08-12gainN0003.fits` gain file. We searched for background flares using data from the S1, since the cluster emission fills the S3. We used the script `lc_clean` to clean the data in the same manner as done by M. Markevitch for the blank sky fields. This script calculates the mean background rate after binning the data into bins with a maximum length of 259.28 seconds (as for the blank sky data) and clips data that are more than 1.2 times different than the mean. A total of 383 seconds of data were excluded using this technique, leaving a total exposure of 28,360 seconds.

3. X-RAY IMAGE

The entire field of view of the ACIS-S3 CCD is shown in Figure 1. The image is in the 0.3 – 10.0 keV band. It is unsmoothed and has not been corrected for background or exposure. The cluster shows substructure in the center. The central bright region is roughly elongated NE to SW, and there is an X-ray deficit to the east of the center. This elongation is approximately aligned with the position angle of the central cD galaxy, as seen in the optical band (see Fig. 2).

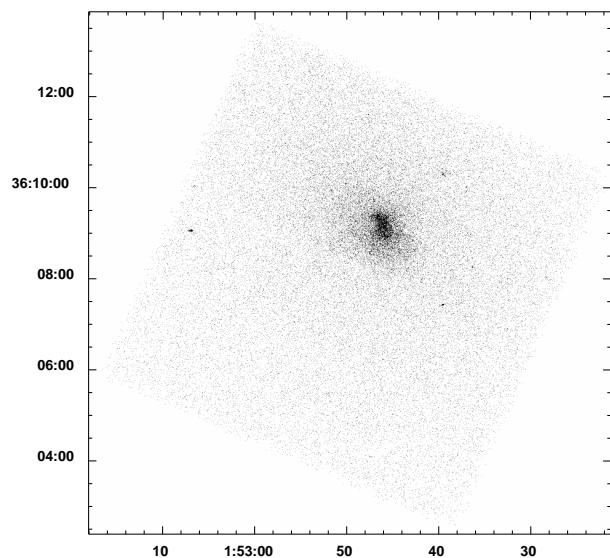


FIG. 1.— Raw *Chandra* ACIS-S3 image of Abell 262. The image is in the 0.3 – 10.0 keV band and has not been corrected for background or exposure. The central region is roughly elongated NE to SW, and there is a deficit in the surface brightness to the east of the center. The x and y axes are RA (J2000) and Dec (J2000), respectively.

Individual sources were detected using the wavelet-detection algorithm WAVDETECT in CIAO. The source detection threshold was set at 10^{-6} , implying that $\lesssim 1$

⁴ <http://asc.harvard.edu/contrib/maxim/bg/>

false source (due to a statistical fluctuation) would be detected within the area of the S3 image. Sources were visually confirmed on the X-ray image. All sources with a signal-to-noise ratio (SNR) less than three were excluded from the final list, including low-level, very extended detections at the edges of the CCD. The final list includes 17 sources, including four sources in the center of the cluster. Some of the sources in the center are likely regions of clumpy ICM rather than discrete X-ray sources. Source positions were compared with optical positions from the USNO-A2.0 catalog (Monet et al. 1998). One of the X-ray sources in the center is $2''.68$ arcsec away from the USNO position of the central cD galaxy, NGC 708. This same X-ray source is $1''.81$ away from the radio core of B2 0149+35 as measured with A-array VLA observations in Fanti et al. (1986). Another X-ray source is $0''.4$ away from an object in the USNO catalog. It is identified as NGC 703, a cluster galaxy to the NW of the central galaxy, which is also a radio source, as seen in the NRAO VLA Sky Survey (NVSS; Condon et al. 1998), with a flux density of 8.3 mJy. There is one additional match with an unidentified optical source in the western part of the field, with an offset of $1''.07$. Since the offsets between the positions measured in the X-ray vs. those measured in the optical and radio are small and not systematic, we have not altered the astrometric solution for the *Chandra* data. An optical image from the Second Generation Red Digitized Sky Survey⁵ (DSS), trimmed to show the same field-of-view as the ACIS-S3 image, is shown in Figure 2. Detected X-ray sources are indicated with circles on the DSS image. The linear feature in the lower right is a defect on the DSS plate.

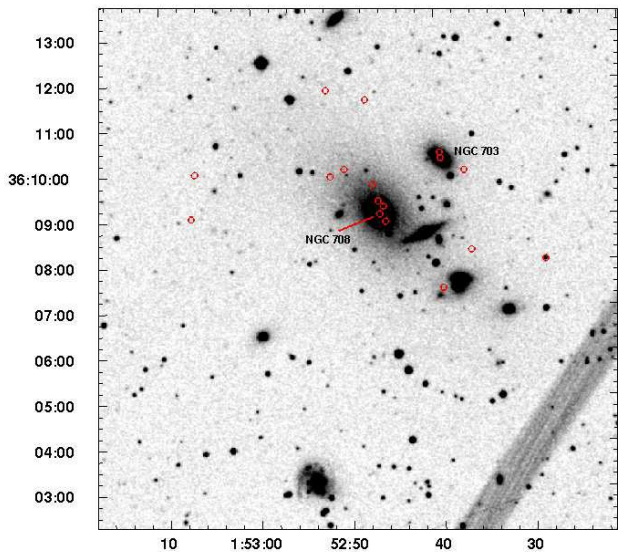


FIG. 2.— Image from the Digitized Sky Survey (DSS), trimmed to match the field-of-view shown in Figure 1. The positions of detected discrete X-ray sources are marked with circles. The feature in the lower right corner is a defect on the DSS plate.

4. CENTRAL REGION OF THE CLUSTER

An adaptively-smoothed image of the central 512×512 pixel (252×252 arcsec; 84×84 kpc) region of the cluster is shown in Figure 3. This image was created with the CIAO task CSMOOTH using a minimum signal-to-noise ratio of 3 per smoothing beam. It was corrected for background and exposure, with the background data taken from the blank-sky images in the CALDB, contributed by M. Markevitch.

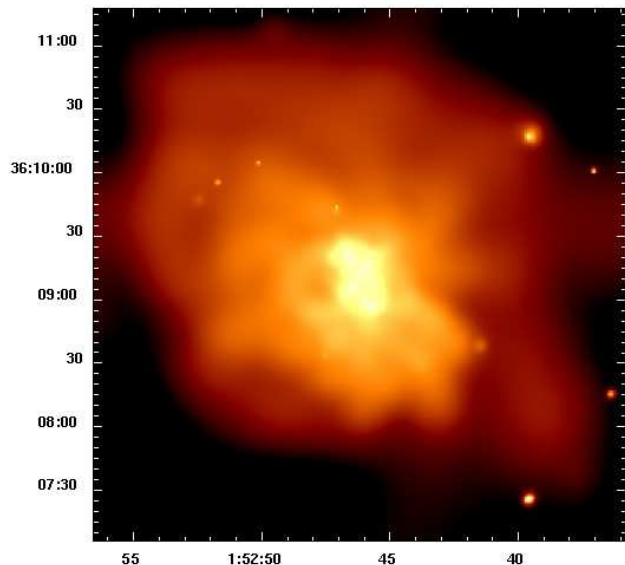


FIG. 3.— Adaptively-smoothed image of the central 252×252 arcsec (84×84 kpc) region of Abell 262. The image has been corrected for background and exposure. Several structures are visible in the image, including a clear “hole” or “bubble” in the emission approximately $10''$ east of the cluster center.

The image shows a variety of structures, including individual point sources, bright knots and filaments of emission, and regions of surface brightness deficit, including a clear “hole” or “bubble” in the emission just east of the center of the cluster. The central approximately $30''$ region contains four bright knots of emission, including a source coincident with the radio core, which may be due to the AGN. To examine this possibility, we have determined the hardness ratios for the “AGN” component and the sum of the three other knots. We define the hardness ratio as $(H-S)/(H+S)$ where H is the number of counts in the 1–10 keV range, and S is the number of counts in the 0.3–1 keV range. Using the blank-sky background data to subtract the background, we find a hardness ratio of 0.14 ± 0.08 for the possible AGN and -0.13 ± 0.05 for the sum of other three knots. Therefore, the hardness ratio for the former is significantly harder than the latter, and probably is due to an additional non-thermal, hard emission component from the AGN. These ratios include all emission along the line of sight towards the AGN and the knots, since the blank sky files were used for the background. If we instead take the background locally in annuli surrounding the extrac-

⁵ The Digitized Sky Surveys were produced at the Space Telescope Science Institute under U.S. Government grant NAG W-2166. The images of these surveys are based on photographic data obtained using the Oschin Schmidt Telescope on Palomar Mountain and the UK Schmidt Telescope. The plates were processed into the present compressed digital form with the permission of these institutions.

tion apertures for each region of interest, we find hardness ratios of $1.0_{-2.0}^{+0.0}$ for the AGN and $-0.40_{-0.35}^{+0.53}$ for the sum of the other knots. The errors are much larger in this case, since the net counts are greatly reduced when subtracting the background locally, and in fact, when doing this, the net soft counts for the AGN are only 0.04 ± 9.7 . Finally, if we examine the hard (1 – 10 keV) and soft (0.3 – 1) keV images, side by side, it is evident that the AGN component includes hard emission that the other knots do not (see Figure 4).

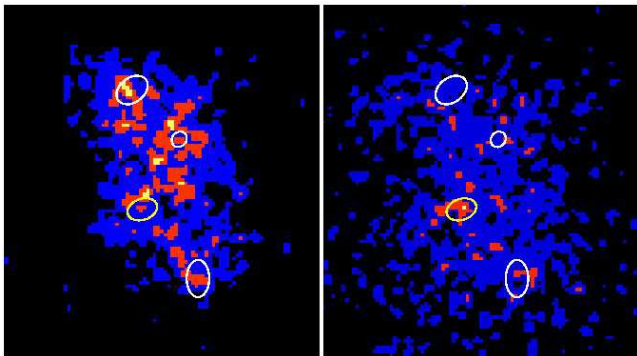


FIG. 4.— Slightly (1 pixel) Gaussian-smoothed images in the soft (0.3 – 1.0 keV; left panel) and hard (1.0 – 10.0 keV; right panel) bands of the central $45'' \times 50''$ region of Abell 262. The positions of the AGN and the other bright knots are marked with yellow and white elliptical regions, respectively, as found with WAVDETECT. The AGN is significantly harder than the other knot regions.

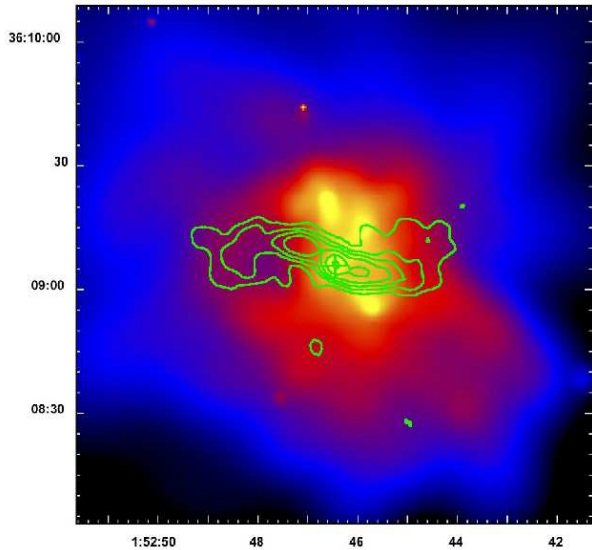


FIG. 5.— Adaptively-smoothed *Chandra* image of the central 125×125 arcsec region of Abell 262 with radio contours at 1.4 GHz (Parma et al. 1986) overlaid. The radio emission is generally anti-correlated with the X-ray emission; this is most clearly seen to the east of the cluster center, where the radio lobe has evacuated a cavity in the X-ray-emitting ICM.

4.1. Radio Source / ICM Interaction

The 1.4 GHz radio contours of B2 0149+35 (Parma et al. 1986) are overlaid onto the adaptively-smoothed *Chandra* image of the central (125×125 arcsec) region of Abell 262 in Figure 5. The radio data are from the VLA in

B configuration and have a resolution of $\sim 3''5$. The total 1.4 GHz flux from the radio source is 78 mJy. This gives a power at 1.4 GHz of $P_{1.4} = 4.7 \times 10^{22} \text{ W Hz}^{-1}$, classifying the source as a fairly weak, double-lobed FR I (Fanaroff & Riley 1974). The largest-angular-size of the radio source is $58'' = 19.2 \text{ kpc}$. The radio source is much less luminous and physically smaller than other similar objects that have had their environments well-studied with *Chandra* data, such as Hydra A (McNamara et al. 2000), 3C 84 in the Perseus cluster (Fabian et al. 2000), and 3C 317 in Abell 2052 (Blanton et al. 2001, 2003).

In Figure 5, an anti-correlation between the radio and X-ray emission is apparent. This is most clearly seen to the east of the cluster center where the radio lobe has “blown a bubble” in the ICM. The radio lobe fills a region of low-surface brightness in the X-ray image and is surrounded by an X-ray-bright shell of emission. This bubble has an inner diameter of $15''.5 = 5.2 \text{ kpc}$. The AGN is visible as a point source in the X-ray that is coincident with the radio core.

4.2. Correlation with [N II] Emission

Contours of [N II] optical line emission at 6584 \AA are superposed onto the adaptively-smoothed *Chandra* image of Abell 262 in Figure 6. The optical data are from Plana et al. (1998). Overall, the [N II] emission is positively correlated with the X-ray emission, and the [N II] emission has extensions that correspond with the X-ray-bright knots of emission in the center of the cluster. The [N II] emission represents gas at a temperature of approximately 10^4 K , and may indicate that at least some of the gas is cooling to low temperatures in these regions. In addition, this argues that the emission from the X-ray knots is thermal in nature. Similar correspondences between X-ray and optical line emission have been seen in the Abell 2052 (Blanton et al. 2001) and Abell 1795 (Fabian et al. 2001b) clusters.

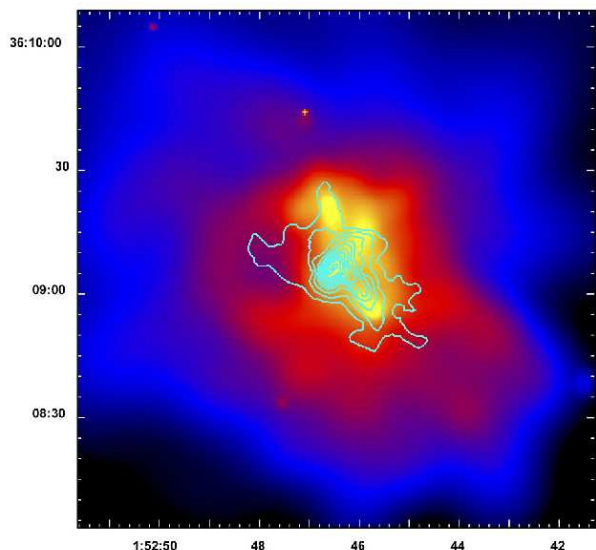


FIG. 6.— Contours of [N II] optical line emission superimposed onto the adaptively-smoothed central region of the *Chandra* image of Abell 262. In general, the [N II] emission is positively correlated with the X-ray emission, and particularly with the X-ray-bright knots, suggesting that cooling to low temperatures is occurring in these regions.

4.3. Temperature Map

A temperature map covering the same region shown in Figures 5 and 6 is displayed in Figure 7. This map was obtained by fitting individual spectra with ISIS in the 0.7 – 8.0 keV band, with the requirement that each spectrum contain a minimum of 1050 counts, including background. Ancillary response function (arf) files were corrected for the low-energy quantum efficiency (QE) degradation in the ACIS-S3 using CORRARF. Point sources were removed before creating the map. The three thermal “knots” of emission that were detected with WAVDETECT were kept in the image, since they most likely represent dense regions of gas, rather than point sources. When constructing the map, each spectrum was binned to a minimum of 20 cts/bin before fitting with a model including Galactic absorption fixed to $5.46 \times 10^{20} \text{ cm}^{-2}$ (Dickey & Lockman 1990), and a thermal plasma model (WABS*MEKAL). The map is an array of 25×25 boxes covering a total of 256×256 pixels. The size of each box is $5'' \times 5''$. Each box does not represent the total size of the region covered by an individual spectral fit, but rather, the center of the region from which a spectrum was extracted and fitted, with the requirement that the region contain at least 1050 counts.

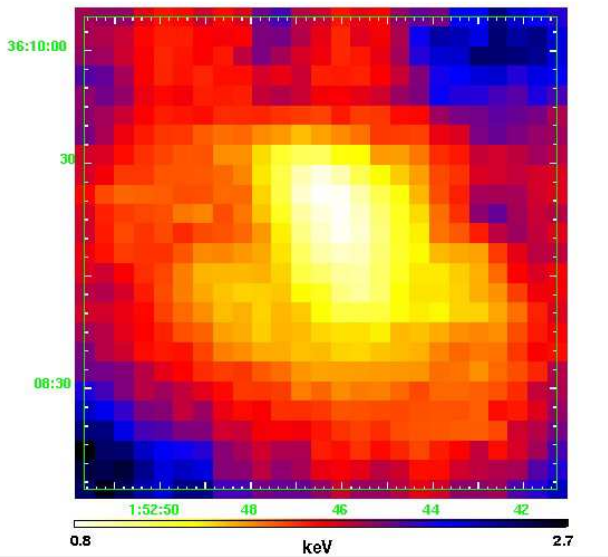


FIG. 7.— Temperature map of the central 125×125 arcsec region of Abell 262. The gas is coolest in the center, with a temperature of 0.8 keV, and rises to 2.7 keV farther out; the color scale shown is linear. The gas surrounding the radio bubble to the east of the center is cool, and shows no sign of being shocked.

The map shows a range of temperatures from 0.8 to 2.7 keV, with the coolest gas found in the center of the cluster, consistent with the temperature distribution predicted from cooling flow models. Errors on the temperature values are typically 10 – 15%. Cool gas is found in the rim of the bubble evacuated from the radio source to the east of the cluster center. This is inconsistent with the temperature distribution expected if the radio lobe was strongly shocking the ICM. Therefore, there is no evidence that the radio lobes are currently providing heat to the ICM through strong shocks, although energy may still be transported through slower expansion of the lobes (see

Reynolds, Heinz, & Begelman 2002). Similar distributions in the gas temperature have been seen in Perseus (Schmidt et al. 2002), Hydra A (Nulsen et al. 2002), and Abell 2052 (Blanton et al. 2003).

5. TOTAL SPECTRUM

A spectrum was extracted from the largest circular region that would fit on the ACIS-S3, centered on the core of the radio source. The region has a radius of $182''$ (60.4 kpc). Point sources detected with WAVDETECT, as described in §3, were excluded. The source coincident with the radio core was excluded, but the three other bright knots of emission in the center were included, since they are thought to be thermal in nature. The spectrum was extracted, and weighted response functions for the region were calculated using the CIAO ACISSPEC script. Since this script only became available with CIAO 2.3, we use this version of CIAO for the spectral analysis. The gain file we used remained unchanged from CIAO 2.2 to CIAO 2.3. The spectral data were grouped to have a minimum of 20 cts/bin. The CIAO script ACISABS was applied to correct for the low-energy quantum efficiency (QE) degradation in the ACIS-S3. The blank-sky observations included in the CALDB and contributed by M. Markevitch were used to extract a background spectrum in the same manner and from the same region described above.

A number of fits were made to the spectrum using XSPEC v11.2.0bg. We fitted single-temperature (1-MEKAL) thermal plasma models, two-temperature (2-MEKAL) models, and cooling flow models (MKCFLOW+MEKAL). In each case, the absorption was fixed to the Galactic value of $5.46 \times 10^{20} \text{ cm}^{-2}$ (Dickey & Lockman 1990), and then allowed to vary. We fitted the spectrum in the 0.7 – 8.0 keV range, excluding the 1.8 – 2.1 keV region that is adversely affected by a feature produced by the iridium coating of *Chandra*’s mirrors. A total of 77,972 counts were detected in the spectrum in the energy range we used for our fits. A systematic error of 2% was added to all of the fits to include the effects of uncertainties in the calibration. The results of the spectral fits are summarized in Table 1.

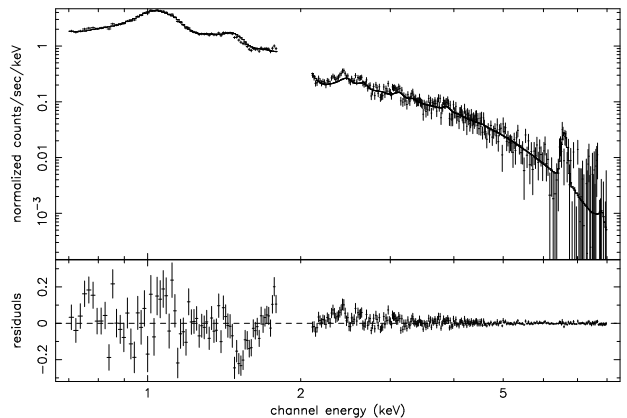


FIG. 8.— Total spectrum for Abell 262, extracted from a circular region with a radius of $182''$ (60.4 kpc) centered on the radio core. The model shown fitted to the spectrum is a cooling flow model with Galactic absorption (MKCFLOW+MEKAL-1), with parameters as listed in Table 1. The 1.8 – 2.1 keV region has been excluded because it is affected by an iridium feature resulting from *Chandra*’s mirror coating.

For the single-temperature fit (1-MEKAL), the average temperature of the cluster is $kT = 1.77_{-0.080}^{+0.025}$ keV, and the average abundance is $0.40_{-0.022}^{+0.016}$ times the solar value. However, this fit clearly does not adequately describe the data. The reduced χ^2 value is 2.60. The fit is improved when the absorption is allowed to vary (1-MEKAL-abs). This results in an absorbing column which is lower than the Galactic value, which we consider unlikely. The low fitted absorption may be due to uncertainties in the correction for the low-energy QE degradation or to additional cooler emission components. The fit is significantly improved with the addition of a second thermal component (2-MEKAL). In this case, the best-fitting low and high temperatures are $kT_{\text{low}} = 1.11_{-0.035}^{+0.024}$ keV, and $kT_{\text{high}} = 2.36_{-0.067}^{+0.074}$ keV, respectively. The average abundance is $0.67_{-0.059}^{+0.055}$ times the solar value. The reduced χ^2 value drops to 1.62 for this fit. The two-temperature fit is slightly improved when the absorption is allowed to vary (2-MEKAL-abs). Here, again, the best fitting value for the absorption is below the Galactic value, but not as much so as for the single-temperature fit.

We fitted the spectrum with a series of cooling flow models, that also include an additional MEKAL component to account for the projection of any outer non-cooling gas in the cluster onto the cooling region. In each case, the higher temperature (kT_{high}) in the cooling flow model (MKCFLOW) was set to be equal to the temperature of the MEKAL component, under the assumption that the MEKAL component represents ambient cluster gas, and that the cooling flow gas is cooled ambient gas. Similarly, the abundance values for the two models were constrained to be equal. The fits were performed with the absorption both fixed to the Galactic value and allowed to vary, as above. In addition, the low temperature component (kT_{low}) was either allowed to vary, or fixed to a very low temperature (0.08 keV) to constrain the amount of gas cooling down to very low temperatures. The fits were better when the low temperature component was allowed to vary freely. These fits indicate that the gas is cooling over only a limited temperature range, from approximately 2.7 to 0.9 keV, similar to the range seen in the temperature map. For the fixed absorption case (MKCFLOW+MEKAL-1), the best-fitting lower and upper temperatures are $0.87_{-0.047}^{+0.096}$ keV and $2.65_{-0.18}^{+0.17}$ keV, respectively, and the mass-deposition rate over this limited temperature range is $\dot{M} = 18.8_{-4.5}^{+5.7} M_{\odot} \text{ yr}^{-1}$. The abundance for this fit is $0.66_{-0.063}^{+0.064}$ times the solar value, and the reduced χ^2 value (1.61) is only slightly better than the 2-MEKAL fit. The free-absorption case (MKCFLOW+MEKAL-abs1) yields similar results, and an absorption value consistent with the Galactic value within the errors. When the low-temperature component is fixed to $kT = 0.08$ keV and the absorption is fixed to Galactic (MKCFLOW+MEKAL-2), the mass-deposition rate drops to $\dot{M} = 5.0_{-0.6}^{+0.5} M_{\odot} \text{ yr}^{-1}$. This suggests that approximately 19 $M_{\odot} \text{ yr}^{-1}$ are cooling over the limited temperature range of 2.7 to 0.9 keV, with only approximately 5 $M_{\odot} \text{ yr}^{-1}$ cooling to very low temperatures (0.08 keV). If the absorption is allowed to vary with the low temperature fixed to 0.08 keV (MKCFLOW+MEKAL-abs2), the mass-deposition rate to very low temperatures in-

creases to $\dot{M} = 11.7_{-1.4}^{+1.8} M_{\odot} \text{ yr}^{-1}$. However, this requires a very high absorption value ($N_H = 14.1_{-1.45}^{+1.79} \times 10^{20} \text{ cm}^{-2}$) to absorb out the expected emission predicted from the cool gas at low energies, and the fit is significantly worse than the cooling flow models where the low-temperature component is allowed to vary. The best fit model is MKCFLOW+MEKAL-1, where the absorption is fixed to the Galactic value, and the gas cools over only a limited temperature range from 2.7 to 0.9 keV. A plot of this model fitted to the spectrum is shown in Figure 8. We note that this fit is only slightly better than the 2-MEKAL model.

6. RADIO BUBBLES

As described in Section 4.1, there is a depression in the X-ray surface brightness to the east of the AGN. This depression is coincident with the eastern radio lobe. The surface brightness in an annular region surrounding the hole is 25% higher, and brighter than the hole at the 4.3σ level. Visually, there seems to be some indication for an additional hole approximately $27''$ east of this one, which may represent a ‘‘ghost cavity’’ as seen in the Perseus cluster (Fabian et al. 2000) and Abell 2597 (McNamara et al. 2001). These may be cavities evacuated from a previous outburst of the radio source. However, this feature is not statistically significant.

We have extracted a spectrum from the outer (eastern) half of the bright shell surrounding the hole that corresponds with the eastern radio lobe. The inner and outer radii of this region are $6''.4$ (2.1 kpc) and $17''.0$ (5.6 kpc), respectively, centered on the hole. The opening angle used for the pie-annulus was 180 degrees. The background spectrum was extracted from a pie-annulus region centered on the AGN and located just exterior to the bright shell in an attempt to subtract off emission along the line-of-sight to the shell from the cluster at radii larger than the bright shell. The spectral data were binned to a minimum of 20 cts/bin and the spectrum was fitted with a model including absorption fixed to the Galactic value and a MEKAL component with the abundance fixed to 0.6 times solar. The fit gave $\chi^2/\text{d.o.f.} = 35.96/40$ and a temperature of $kT = 1.20_{-0.19}^{+0.17}$ keV. Since the normalization of the model is proportional to n_e^2 , we can determine the density and pressure in this region. We assume that the emission for the outer shell region is part of a spherical shell of emission. We find an electron density of $n_e = 0.021 \text{ cm}^{-3}$ and a pressure $P = 8 \times 10^{-11} \text{ dyn cm}^{-2}$. Note that if we take our background spectrum from the blank-sky files in the same region that we extract the shell spectrum, the ‘‘projected’’ pressure is higher, $P = 1.8 \times 10^{-10} \text{ dyn cm}^{-2}$. Following a similar procedure as above, but extracting the spectrum from a full, circular shell surrounding the radio bubble, with inner and outer radii of $7''.8$ (2.6 kpc) and $13''.0$ (4.3 kpc), respectively, and extracting the background locally from a region just east of this shell, we find a pressure $P = 1.2 \times 10^{-10} \text{ dyn cm}^{-2}$. We therefore adopt a pressure value of $P = 1 \times 10^{-10} \text{ dyn cm}^{-2}$. This is a factor of five higher than the pressure determined from the radio observations for the eastern radio lobe of $P_{\text{eq}} = 1.9 \times 10^{-11} \text{ dyn cm}^{-2}$ (Heckman et al. 1989, converted to our cosmology), assuming equipartition of energy. This suggests that there is an additional pressure component in the radio bubble

providing support to the X-ray shell. One possibility for this component is very hot, diffuse thermal gas. A similar pressure discrepancy has been found in other similar objects such as Hydra A (McNamara et al. 2000) and Abell 2052 (Blanton et al. 2001). The isobaric cooling time in this portion of the bright shell is 4.0 (2.8) $\times 10^8$ yr, for the partial (full) shell case, much shorter than the probable age of the cluster. This is consistent with the correlation of cool ($\sim 10^4$ K) gas (see §4.2) with the X-ray-bright regions in the cluster center. The synchrotron age of the radio source, calculated from the 1.4 GHz data presented in Parma et al. (1986), is 3.5×10^7 yr, much shorter than the cooling time. Therefore, the gas in the shell did most of its cooling to its current temperature while it was closer to the center of the cluster, and was then pushed outward by the radio source.

6.1. Energy Injection into the ICM

One of the most promising solutions to the “cooling flow problem” (sufficient quantities of gas are not found at sufficiently low temperatures, as based on expectations from X-ray data) is that energy input from an AGN hosted by a central cluster galaxy can offset the cooling. Even without knowing the details of the mechanism by which this energy is transferred to the ICM, we can test whether the energy output from the radio-emitting AGN is adequate to balance the cooling losses. This has been found to be the case in other objects such as Hydra A (David et al. 2001) and Abell 2052 (Blanton et al. 2003).

The luminosity of isobaric cooling gas is given by

$$L_{\text{cool}} = \frac{5}{2} \frac{kT}{\mu m_p} \dot{M}, \quad (1)$$

where kT is the temperature of the ICM outside of the cooling region, \dot{M} is the cooling rate, and μ is the mean mass per particle in units of the proton mass. Using $kT = 2.65$ keV, and the mass-deposition rate of $18.8 M_{\odot} \text{ yr}^{-1}$, we find $L_{\text{cool}} = 1.3 \times 10^{43}$ erg s^{-1} . We used the mass-deposition rate found in the spectral fit where the low temperature was allowed to vary. This represents gas cooling from 2.65 to 0.66 keV, and for the comparison with the radio source energy, we assume that all of this mass needs to be heated. Using a different method, subtracting the spectroscopically-determined cooling luminosity (with the temperature fixed to a low value) from the morphological measure of the cooling luminosity, Birzan et al. (2004) find a very similar value ($L_{\text{cool}} = 1.2 \times 10^{43}$ erg s^{-1}) for A262. We compare our value of the cooling luminosity with the total energy output from the radio source. Following Churazov et al. (2002), the energy required to inflate the bubble seen in the X-ray is the sum of the internal energy of the bubble and the work done in creating the cavity and compressing the shell

$$E_{\text{rad}} = \frac{1}{(\gamma - 1)} PV + PdV = \frac{\gamma}{(\gamma - 1)} PV, \quad (2)$$

where V is the volume of the cavity, and γ is the mean adiabatic index of the fluid in the cavity. Using $7''8$ (2.6 kpc) as the radius of the hole to the east of the cluster center, and the pressure derived above of $P = 1 \times 10^{-10}$ dyn cm^{-2} , we find $E_{\text{rad}} = 5.3 \times 10^{56}$ erg for nonrelativistic gas ($\gamma = 5/3$, $E_{\text{rad}} = 5/2 PV$) and $E_{\text{rad}} = 8.5 \times 10^{56}$ erg for relativistic gas ($\gamma = 4/3$, $E_{\text{rad}} = 4PV$). We assume that

the western radio lobe is supplying the same amount of energy as the eastern, giving a total energy for both lobes of $E_{\text{rad}} = 1.1 \times 10^{57}$ erg ($E_{\text{rad}} = 1.7 \times 10^{57}$ erg) for $\gamma = 5/3$ ($\gamma = 4/3$). As evidenced by the presence of ghost cavities (holes in the X-ray emission that have risen buoyantly outward from the cluster centers into the ICM) in other cooling flow clusters such as Perseus (Fabian et al. 2000) and Abell 2597 (McNamara et al. 2002), radio sources are episodic with a repetition rate of $\approx 10^8$ yr (derived from the buoyancy rise time of the cavities). Assuming the same repetition rate of radio outbursts in the core of Abell 262, we find that the total power output from the radio source is 3.4×10^{41} erg/s (5.4×10^{41} erg/s) for $\gamma = 5/3$ ($\gamma = 4/3$). This falls more than an order of magnitude short of the necessary average energy output rate required to offset the luminosity of cooling gas in Abell 262. This result is different from that for other well-studied cases such as Hydra A and Abell 2052, where E_{rad} is sufficient to balance cooling. Although the X-ray gas pressures in the centers of all three clusters are similar, the bubble volumes are much greater in Abell 2052 and Hydra A (bubble diameters ≈ 20 kpc) than in Abell 262 (bubble diameter ≈ 5 kpc). In addition, the observed radio powers in the other objects are much higher (by orders of magnitude) than in Abell 262. It may be that some other mechanism (e.g., thermal conduction) balances radiative cooling in Abell 262 rather than heating by the radio source. Alternatively, it is possible that the radio source in Abell 262 is experiencing a less powerful than average outburst, and that previous outbursts were more powerful allowing the radio source to balance the cooling losses on average. Another possibility is that the repetition rate is higher for this radio source than others – a repetition rate of 6×10^6 yr ($\gamma = 5/3$) or 1×10^7 yr ($\gamma = 4/3$) rather than the assumed 10^8 yr would be required. The problem with a rapid repetition rate is that, if the axis of the jets remains fixed, this might simply add to the observed energy content of the present radio bubble. The required repetition time is shorter than the synchrotron lifetime of the radio source of 3.5×10^7 yr, so repeated injections into the same bubble would just add to the observed radio emission. If the buoyancy time of the bubbles were small enough, they might move away between outbursts. Taking the sound speed (500 km s^{-1}) as the upper limit of the buoyancy velocity, the time for a bubble to move one bubble diameter (5 kpc) is $t_{\text{buoy}} > 1 \times 10^7$ yr. A radio source repetition rate that would repeat on a shorter timescale than this (as would be necessary in the above scenario where a more rapid repetition rate supplies the required energy to offset the cooling) would result in more energy being injected into the current bubble which would be detectable in the pressure and volume of the X-ray shell. Therefore, it seems unlikely that a shorter repetition rate would account for the necessary energy required to offset the cooling flow. The more likely possibility is that previous outbursts of the radio source were more powerful, if the radio source is to supply the required energy.

7. CONCLUSIONS

We have presented an analysis of the *Chandra* observation of the central region of the cooling flow cluster Abell 262. Complex structure is found, including bright knots of

emission and a hole in the X-ray emission that is spatially-coincident with the eastern radio lobe associated with the radio source hosted by the central cD galaxy. One of the bright knots of emission is coincident with the core of the radio source, and a hardness ratio analysis indicates that this source includes an emission component from the AGN. The knotty structure seen in the center is located in the same region as optical [N II] line emission, suggesting that gas is cooling down to approximately 10^4 K in these regions. The temperature map shows that these same regions are among the coolest areas in the cluster, with X-ray-derived temperatures of approximately 0.8 keV. The map also shows that the compressed X-ray-emitting gas surrounding the radio bubble is cool, and does not provide evidence of recent shock heating by the radio lobe.

Fitting a number of different models to the total spectrum for the cluster revealed that the best fit is achieved with a cooling flow model with a mass deposition rate of $\dot{M} = 18.8_{-4.5}^{+5.7} M_{\odot} \text{ yr}^{-1}$ and an elemental abundance of $0.66_{-0.063}^{+0.064}$ times the solar value. No evidence is seen for excess absorption. The mass deposition rate is similar to that measured from previous observatories (*ASCA*, White 2000; *ROSAT*, Peres 1998), however we find that the gas cools only over a limited temperature range, by a factor of three from 2.7 to 0.9 keV. This is similar to the result of Peterson et al. (2003) who found $\dot{M} = 10 \pm 1 M_{\odot}$ in the range kT to $kT/2$, where $kT = 2.1 \pm 0.2$ keV, using *XMM-Newton* data.

The radio source in the center of Abell 262, with a 1.4 GHz power of $P_{1.4} = 4.7 \times 10^{22} \text{ W Hz}^{-1}$, is orders of magnitude less luminous than the central sources in other well-studied cooling flows such as Hydra A (McNamara et al. 2000), Perseus (Fabian et al. 2000) and Abell 2052 (Blan-

ton et al. 2001, 2003). The cavity evacuated in the ICM by this source, with a diameter of ≈ 5 kpc, is much smaller than those measured in the other systems just mentioned, which have cavity diameters of approximately 20 kpc. The X-ray pressure measured in the bright shell surrounding the cavity is higher than the radio equipartition pressure, as is found with the other sources. Although the central gas pressures measured in Hydra A (McNamara et al. 2000), Perseus (Schmidt et al. 2002), and Abell 2052 (Blanton et al. 2001, 2003) are all similar to that in Abell 262, the smaller bubble volume in A262 translates into much less energy being injected into the cooling gas by the radio source than in the other systems. A comparison of the energy injected by the radio source and the luminosity of the cooling gas shows that the radio source energy is insufficient to offset the cooling of the gas unless it is experiencing a less powerful than average outburst, and was more powerful in the past.

We thank Joshua Kempner (CfA) and John Houck (MIT), who provided us with their spectral mapping software which was used to create the temperature map. Support for E. L. B. was provided by NASA through the *Chandra* Fellowship Program, grant award number PF1-20017, under NASA contract number NAS8-39073. This research was supported by the National Aeronautics and Space Administration through *Chandra* Award Numbers GO2-3160X and GO3-4155X, issued by the *Chandra* X-ray Observatory Center, which is operated by the Smithsonian Astrophysical Observatory for and on behalf of NASA under contract NAS8-39073. Some support came from NASA *XMM-Newton* Grant NAG5-13089.

REFERENCES

- Birzan, L., Rafferty, D. A., McNamara, B. R., Wise, M. W., & Nulsen, P. E. J. 2004, *ApJ*, in press, astro-ph/0402348
- Blanton, E. L., Sarazin, C. L., McNamara, B. R., & Wise, M. W. 2001, *ApJ*, 558, L15
- Blanton, E. L., Sarazin, C. L., & McNamara, B. R. 2003, *ApJ*, 585, 227
- Churazov, E., Sunyaev, R., Forman, W., & Böhringer, H. 2002, *MNRAS*, 332, 729
- Condon, J. J., Cotton, W. D., Greisen, E. W., Yin, Q. F., Perley, R. A., Taylor, G. B., & Broderick, J. J. 1998, *AJ*, 115, 1693
- David, L. P., Slyz, A., Jones, C., Forman, W., Vrtilek, S. D., & Arnaud, K. A. 1993, *ApJ*, 412, 479
- David, L. P., Jones, C., & Forman, W. 1996, *ApJ*, 473, 692
- David, L. P., Nulsen, P. E. J., McNamara, B. R., Forman, W., Jones, C., Ponman, T., Robertson, B., & Wise, M. 2001, *ApJ*, 557, 546
- Dickey, J. M., & Lockman, F. J. 1990, *ARA&A*, 28, 215
- Fabian, A. C. 1994, *ARA&A*, 32, 277
- Fabian, A. C., Sanders, J. S., Ettori, S., Taylor, G. B., Allen, S. W., Crawford, C. S., Iwasawa, K., Johnstone, R. M., & Ogle, P. M. 2000, *MNRAS*, 318, L65
- Fabian, A. C., Mushotzky, R. F., Nulsen, P. E. J., & Peterson, J. R. 2001, *MNRAS*, 321, L20
- Fabian, A. C., Sanders, J. S., Ettori, S., Taylor, G. B., Allen, S. W., Crawford, C. S., Iwasawa, K., & Johnstone, R. M. 2001b, *MNRAS*, 321, L33
- Fabian, A. C., Sanders, J. S., Allen, S. W., Crawford, C. S., Iwasawa, K., Johnstone, R. M., Schmidt, R. W., & Taylor, G. B. 2003, *MNRAS*, 344, L43
- Fanaroff, B. L., & Riley, J. M. 1974, *MNRAS*, 167, 31P
- Fanti, C., Fanti, R., de Ruiter, H. R., & Parma, P. 1986, *A&AS*, 65, 145
- Forman, W., Nulsen, P., Heinz, S., Owen, F., Eilek, J., Vikhlinin, A., Markevitch, M., Kraft, R., Churazov, E., & Jones, C. 2004, *ApJ*, submitted, astro-ph/0312576
- Heckman, T. M., Baum, S. A., van Breugel, W. J. M., & McCarthy, P. 1989, *ApJ*, 338, 48
- Heinz, S., Reynolds, C. S., & Begelman, M. C. 1998, *ApJ*, 501, 126
- Johnstone, R. M., Allen, S. W., Fabian, A. C., & Sanders, J. S. 2002, *MNRAS*, 336, 299
- McNamara, B. R. 1997, in *Galactic and Cluster Cooling Flows*, ed. N. Soker (San Francisco: PASP), 109
- McNamara, B. R., Wise, M., Nulsen, P. E. J., David, L. P., Sarazin, C. L., Bautz, M., Markevitch, M., Vikhlinin, A., Forman, W. R., Jones, C., & Harris, D. E. 2000, *ApJ*, 534, L135
- McNamara, B. R., Wise, M. W., Nulsen, P. E. J., David, L. P., Carilli, C. L., Sarazin, C. L., O’Dea, C. P., Houck, J., Donahue, M., Baum, S., Voit, M., O’Connell, R. W., Koekemoer, A. 2001, *ApJ*, 562, L149
- Monet, D., et al. 1998, *USNO-A V2.0*, a Catalog of Astrometric Standards (Flagstaff: USNO)
- Neill, J. D., Brodie, J. P., Craig, W. W., Hailey, C. J., & Misch, A. A. 2001, *ApJ*, 548, 550
- Nulsen, P. E. J., David, L. P., McNamara, B. R., Jones, C., Forman, W. R., & Wise, M. 2002, *ApJ*, 568, 163
- Parma, P., de Ruiter, H. R., Fanti, C., & Fanti, R. 1986, *A&AS*, 64, 135
- Peres, C. B., Fabian, A. C., Edge, A. C., Allen, S. W., & Johnstone, R. M. 1998, *MNRAS*, 298, 416
- Peterson, J. R., Paerels, F. B. S., Kaastra, J. S., Arnaud, M., Reiprich, T. H., Fabian, A. C., Mushotzky, R. F., Jernigan, J. G., & Sakelliou, I. 2001, *A&A*, 365, L104
- Peterson, J. R., Kahn, S. M., Paerels, F. B. S., Kaastra, J. S., Tamura, T., Bleeker, J. A. M., Ferrigno, C., & Jernigan, J. G. 2003, *ApJ*, 590, 207
- Plana, H., Boulesteix, J., Amram, Ph., Carignan, C., & Mendes de Oliveira, C. 1998, *A&AS*, 128, 75
- Reynolds, C. S., Heinz, S., & Begelman, M. C. 2002, *MNRAS*, 332, 271

Schmidt, R. W., Fabian, A. C., & Sanders, J. S. 2002, MNRAS, 337,
71
Soker, N., Blanton, E. L., & Sarazin, C. L. 2002, ApJ, 573, 533

White, D. A. 1992, Ph.D. thesis, Cambridge Univ.
White, D. A. 2000, MNRAS, 312, 663

TABLE 1
FITS TO THE TOTAL SPECTRUM

Model	N_H ($\times 10^{20}$ cm $^{-2}$)	kT_{low} (keV)	kT_{high} (keV)	Abund (solar)	\dot{M} (M_{\odot} yr $^{-1}$)	$\chi^2/\text{d.o.f.}$
1-MEKAL	(5.46)	...	$1.77^{+0.025}_{-0.0080}$	$0.40^{+0.016}_{-0.022}$...	882.4/340=2.60
1-MEKAL-abs	$1.98^{+0.85}_{-0.41}$...	$1.98^{+0.045}_{-0.027}$	$0.55^{+0.020}_{-0.034}$...	859.0/339=2.53
2-MEKAL	(5.46)	$1.11^{+0.024}_{-0.035}$	$2.36^{+0.074}_{-0.067}$	$0.67^{+0.055}_{-0.059}$...	547.8/338=1.62
2-MEKAL-abs	$3.55^{+1.38}_{-0.67}$	$1.16^{+0.16}_{-0.060}$	$2.45^{+0.19}_{-0.10}$	$0.68^{+0.038}_{-0.087}$...	542.5/337=1.61
MKCFLOW+MEKAL-1	(5.46)	$0.87^{+0.096}_{-0.047}$	$2.65^{+0.17}_{-0.18}$	$0.66^{+0.064}_{-0.063}$	$18.8^{+5.7}_{-4.5}$	543.8/338=1.61
MKCFLOW+MEKAL-abs1	$3.95^{+1.76}_{-0.69}$	$0.96^{+0.039}_{-0.14}$	$2.87^{+0.70}_{-0.35}$	$0.66^{+0.054}_{-0.066}$	$21.4^{+3.4}_{-5.9}$	541.8/337=1.61
MKCFLOW+MEKAL-2	(5.46)	(0.08)	$2.16^{+0.074}_{-0.028}$	$0.75^{+0.072}_{-0.050}$	$5.0^{+0.5}_{-0.6}$	675.5/339=1.99
MKCFLOW+MEKAL-abs2	$14.10^{+1.79}_{-1.45}$	(0.08)	$2.21^{+0.075}_{-0.042}$	$0.82^{+0.066}_{-0.072}$	$11.7^{+1.8}_{-1.4}$	582.8/338=1.72